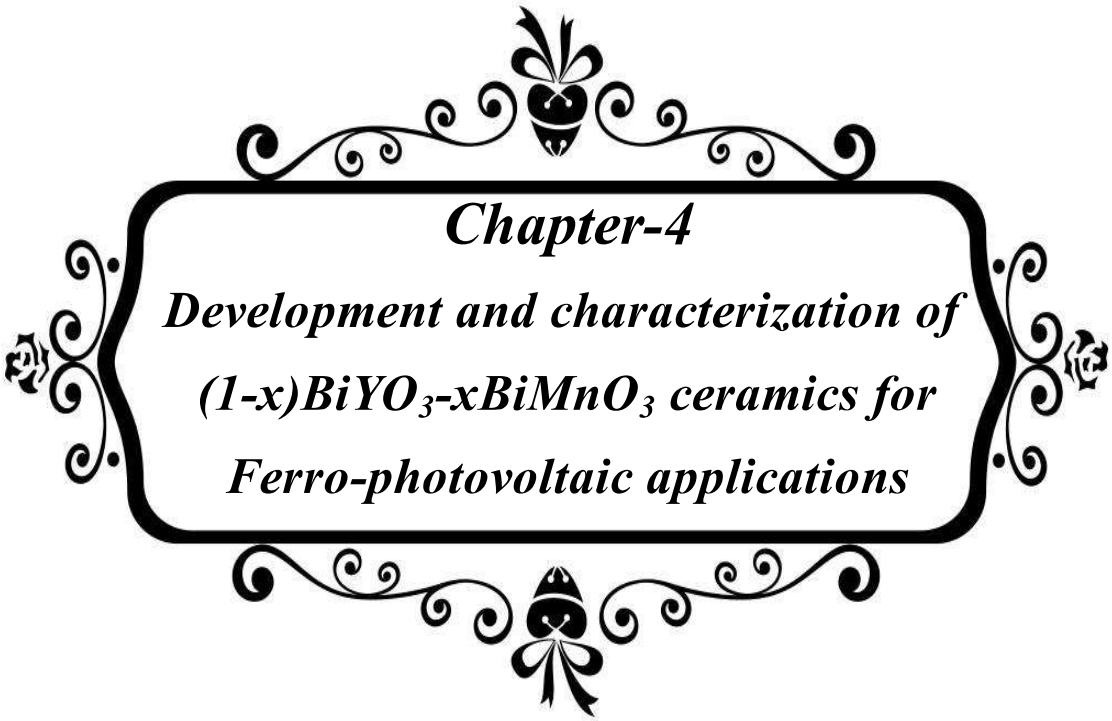

# *Chapter-4*

## *Development and characterization of $(1-x)BiYO_3$-$xBiMnO_3$ ceramics for Ferro-photovoltaic applications*

## 4.1. Introduction

As discussed in chapter 1, the wide band gap (above 3.0 eV) and poor DC-conductivity are the challenging limitations in the typical ferroelectrics like $PbTiO_3$, $BaTiO_3$, $PbZr_xTi_{1-x}O_3$ and hence various attempts are reported e.g. $Ba_{0.95}Ca_{0.05}Ti_{0.92}Sn_{0.08-x}Zr_xO_3$, $BaTiO_3$-$_xBaCo_{0.5}Nb_{0.5}O_{3-\delta}$ etc. to reduce the band gap for PV applications [22, 45, 164-166]. The wide band gap results due to large electronegativity difference between B-site transition metal cation and oxygen ion [19]. As a potential PV material, $BiFeO_3$ is the highly investigated system due to relatively lower band gap (2.67 eV) and high polarization than other typical ferroelectric oxides [167, 168]. The Bi-based perovskite ferroelectrics are more promising than Pb-based perovskites, due to presence of similar $6s^2$ lone-pair in $Bi^{3+}$ ion for purpose of lead-free materials, but still the band gap is not low enough to absorb the large range (more than 80%) of solar spectrum [164, 169, 170].

In this chapter, good absorptivity of $BiYO_3$ ceramics and ferroelectric properties of $BiMnO_3$ is aimed to be combined in one material in the form of their solid solutions as $BiY_{(1-x)}Mn_xO_3$ (BYM). The $BiMnO_3$ is a multiferroic material where ferroelectricity originates due to lone pair of Bi at A-site, which persists upto ferroelectric transition temperature $T_c$ = 425K. Bismuth ferrite is also a Bi based material where ferroelectricity originates due to lone pair, is reported to give large photovoltage ~ 15V [171, 172]. Reduction in band gap as well as improvement in ferroelectricity by Mn doping is reported in many perovskite ferroelectrics such as Mn doped $BiFeO_3$ [173, 174], Sr-Mn doped $BiFeO_3$ [175]. The $BiMnO_3$-$K_{0.5}Na_{0.5}NbO_3$ solid solution [176] and Mn-Nb co doped $BaTiO_3$ [177] also showed significant reduction in band gap even though with partial loss in polarization. It is expected that in BYM, hybridization of O-2p with either of Bi-6s or Mn-3d or both will shift the

maxima of valence band to upper side resulting in reduction of band gap [178]. Moreover, presence of orbitals with energy levels just higher than the valence band can provide multiple absorption and exhibit multiple absorption edges [179-181]. Therefore, strategy of using different concentration of 'Mn' and 'Y' at the B-site, in Bi-containing oxide fluorite BYM system, can lead to significantly efficient ferroelectric photovoltaic material. To the best of our knowledge, such combination of 'Mn' and 'Y' at B-site in oxide perovskites, is not reported yet.

**4.2. Experimental:**

Pure $BiMnO_3$ phase powder is difficult to synthesis in perovskite phase by conventional solid-state method without applying high pressure synthesis [182, 183] and many attempts for synthesis of single phase $BiMnO_3$ by high energy ball milling method are reported in literature [184, 185] . In view of this, high energy ball milling has been adopted, which should be more suitable for synthesis of different compositions of $BiY_{(1-x)}Mn_xO_3$ ($x$ = 0.0, 0.10, 0.25, 0.50, 0.75) solid solution [184]. Stoichiometric amounts of analytical reagent (AR) grade $Bi_2O_3$ (Hi-media, 99%), $Y_2O_3$ (Sigma Aldrich, 99.99%) and $Mn(CH3COO)_2.4H_2O$ (Sigma Aldrich, 99%) were mixed mechanically in ethanol medium for 20 hours. Excess 2% $Bi_2O_3$ reactant were taken to compensate for Bismuth loss at high temperature during calcination and sintering. Reactants of all the samples were mixed at 300 rpm by high energy ball milling, using Retsch PM-400MA planetary ball mill, keeping sample to ball weight ratio as 1:10. The homogeneous mixture of milled powder was heated about 100°C to evaporate the milling media (ethanol) and then calcined. Optimization of calcination condition was done in a muffle furnace in air atmosphere by calcining at different temperatures and different durations. The optimum calcination temperature was determined to be 800°C

for 4 hours duration. Pellets of calcined powders were prepared with the help cylindrical steel die using 2% water solution of PVA as binder and pressing at 7-ton. The sintering of pellets was done at 900°C for 2 hours inside sealed alumina crucible. Thermal behavior of the uncalcined (mixture obtained after milling) sample were investigated by Mettler Toledo thermo-gravimetric and differential thermal analyser (TG-DTA) in the temperature range 40-800°C at the heating rate of 10°C/min. Structural phase formation and phase analysis were done by X-ray diffraction (XRD) data. The XRD measurement was done in the 2θ range 10°-90° at the 2θ steps of 0.02° using Cu-based Rigaku Miniflex, x-ray powder diffractometer. Le-Bail full pattern matching refinements were carried out for structural analysis from XRD data, using FullProf suite software package. For microstructural analysis, surface images were taken by ZEISS EVO 18 scanning electron microscope. Temperature dependent dielectric response was recorded by KEYSIGHT–E4990A impedance analyzer. K-Alpha Thermo Fisher Scientific XPS is used to determine the oxidation states of Bi, Mn, Y and Oxygen. Analysis of the XPS spectra for various elements were carried out using XPSPEAK4.1 software. Spectral characteristic was studied after recording the diffuse reflectance spectra by the SHIMADZU UV-2600 UV-Vis spectrophotometer. Ferroelectric polarization (P)-electric field (E) hysteresis loop of all the compositions were recorded with the help of Radiant Precision Premier II ferroelectric tester.

### 4.3. Results and Discussion

#### 4.3.1. Thermal Analysis

Fig. 4.1 shows the Differential Thermal Analysis (DTA) and Thermo Gravimetric (TGA) curves of uncalcined $BiY_{0.50}Mn_{0.50}O_3$ sample in the temperature range 40°C to 800°C. It can be seen that there are two steps in the weight loss curve, one around 80°C (~8% loss) and other around 320°C (~20%). The first weight loss

around 80°C, without any change in heat flow can be interpreted as loss of remaining ethanol or moisture. The second weight loss around 320°C followed by an endothermic peak in heat flow corresponds to the removal of water of crystallization and decomposition of organic components present in the $Mn(CH3COO)_2.4H_2O$ raw material. A broad endothermic peak in DTA curve in the range of 450°C to 650°C with slight increase in weight can be related to the solid-state reaction of reactants along with the formation of phase and beginning of crystallization. Slight upward trend in the TGA curve at higher temperatures may correspond to the addition of oxygen from the atmosphere to fulfill the lack of oxygen and consequent weight gain [186, 187]. It is evident from TGA and heat flow curves that the phase formation process is almost complete around 700°C. Thus, calcination temperature should be chosen above this temperature for phase pure samples consistent with the previous reported calcination temperature in similar systems [179].

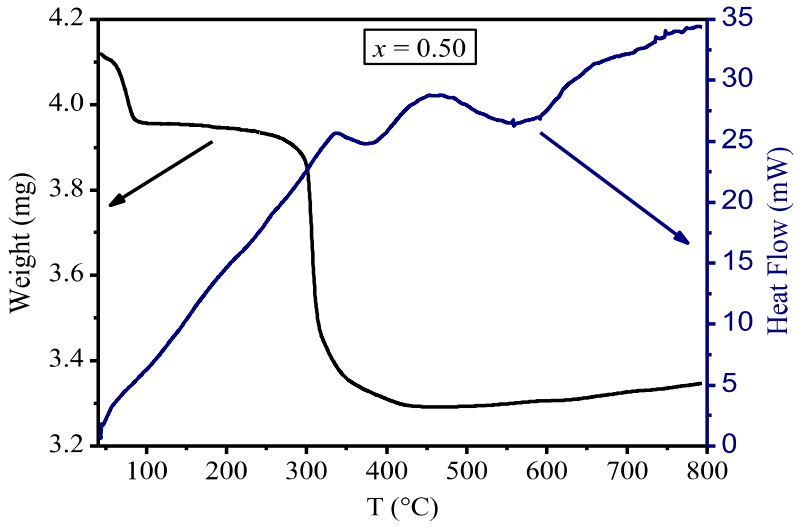


**Figure 4.1:** TGA and DTA graphs of uncalcined $BiY_{(1-x)}Mn_xO_3$ ( $x$ = 0.50 ) sample.

### 4.3.2. Microstructural Characterization:

Figs. 4.2 (a, b, c and d) show the scanning electron microscope (SEM) images of the as sintered ceramic pellets with compositions x=0, 0.10, 0.25, and 0.75,

respectively. It should be noted that the micrograph magnification for x=0, 0.10, 0.25 is 25KX, while it is 20KX for x=0.75 (Fig. 4.2(g)). For all the compositions, the surface morphology appears to be homogeneous, non-porous having rounded grains with merged boundaries. It reveals the formation of liquid phase during sintering due to local melting of the Bi containing phase. The energy dispersive spectroscopy (EDS) spectra for one composition with $x$ = 0.75 is shown in Fig. 4.2(e). The EDS spectra confirms the presence of all the elements Bi, Mn, Y and O and their atomic ratio are in good agreement with the nominal composition. The SEM micrograph of pure $BiYO_3$ (x=0) sample shows more closely packed and relatively smaller grains in comparison to the higher Mn compositions. The x=0 sample, exhibits a floury looking morphology consisting of uniform particles (see Fig. 4.2(a)) whereas the Mn-containing samples, show clear grain formation of different sizes with merged grain boundaries. The composition with x=0.10 has almost uniform grain size distribution with multiple grains of average size 0.45 μm while some melted larger grains are also seen. The melted larger grains are well resolved in SEM image of the fractured surface (see Fig. 4.2(g)). The composition x=0.25 has bimodal microstructure with two range of grain sizes, the larger grains of estimated average size 1.4 μm are surrounded with smaller grains of average size 0.4 μm. For the composition with x=0.75, instead of uniform distinct grains, agglomerated particle like structure can be seen on the surface. To verify that whether the local melting of grains is confined to the pellet surface only or present in interior grains too, we recorded the SEM image of the fractured inner pellet surface as well. Fig. 4.2 (f-i) shows SEM images of the fractured surface from inner cross section of $BiY_{(1-x)}Mn_xO_3$ for x = 0, 0.10, 0.25 and 0.75 recorded at the same (25KX) magnification.

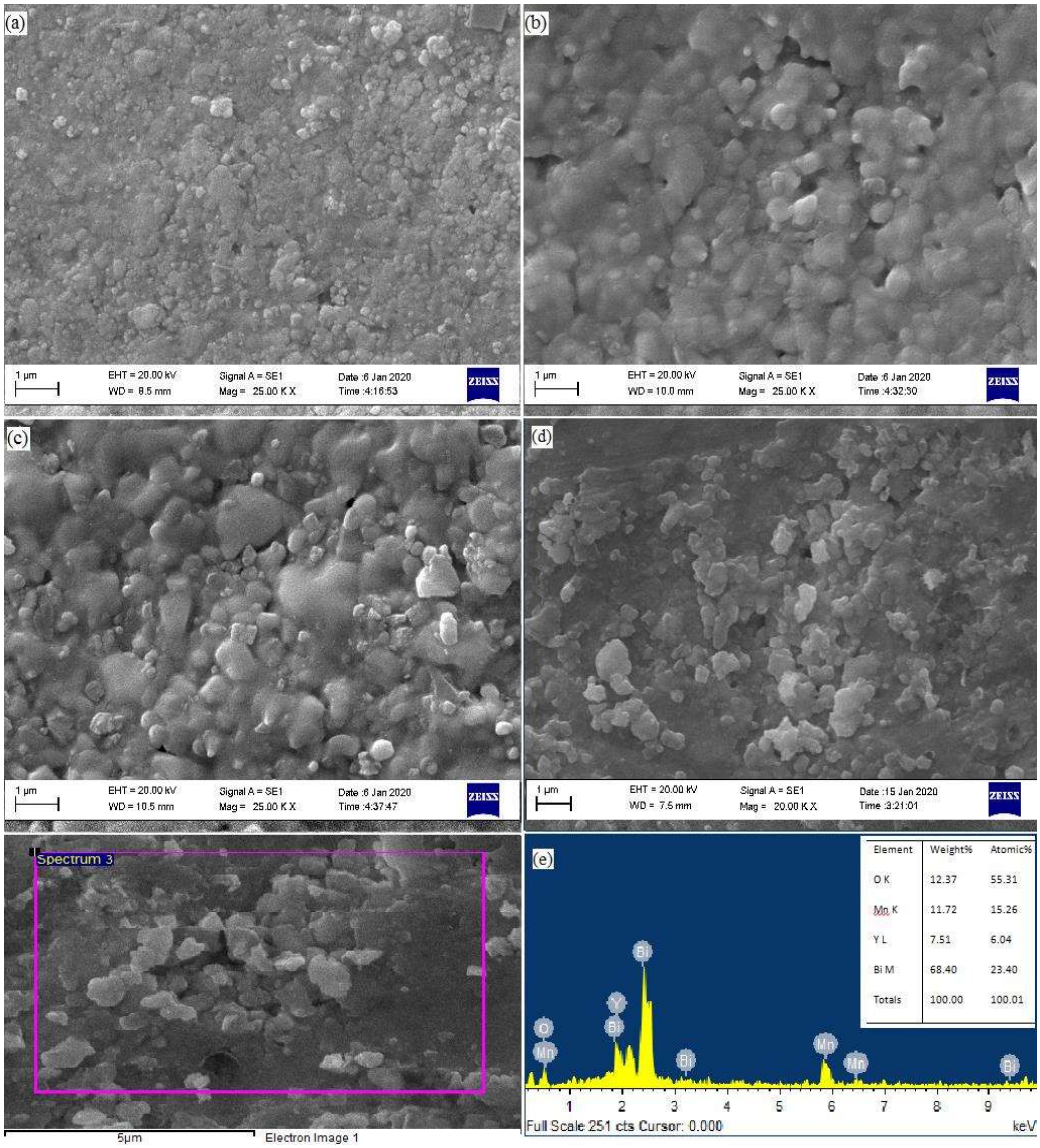


**Figure 4.2:** SEM micrographs of $BiY_{(1-x)}Mn_xO_3$ pellets sintered at 900°C for two hour (a) $x = 0.0$ (b) $x = 0.10$ (c) $x = 0.25$ (d) $x = 0.75$ and (e) EDX spectrum of $x = 0.75$ sample.

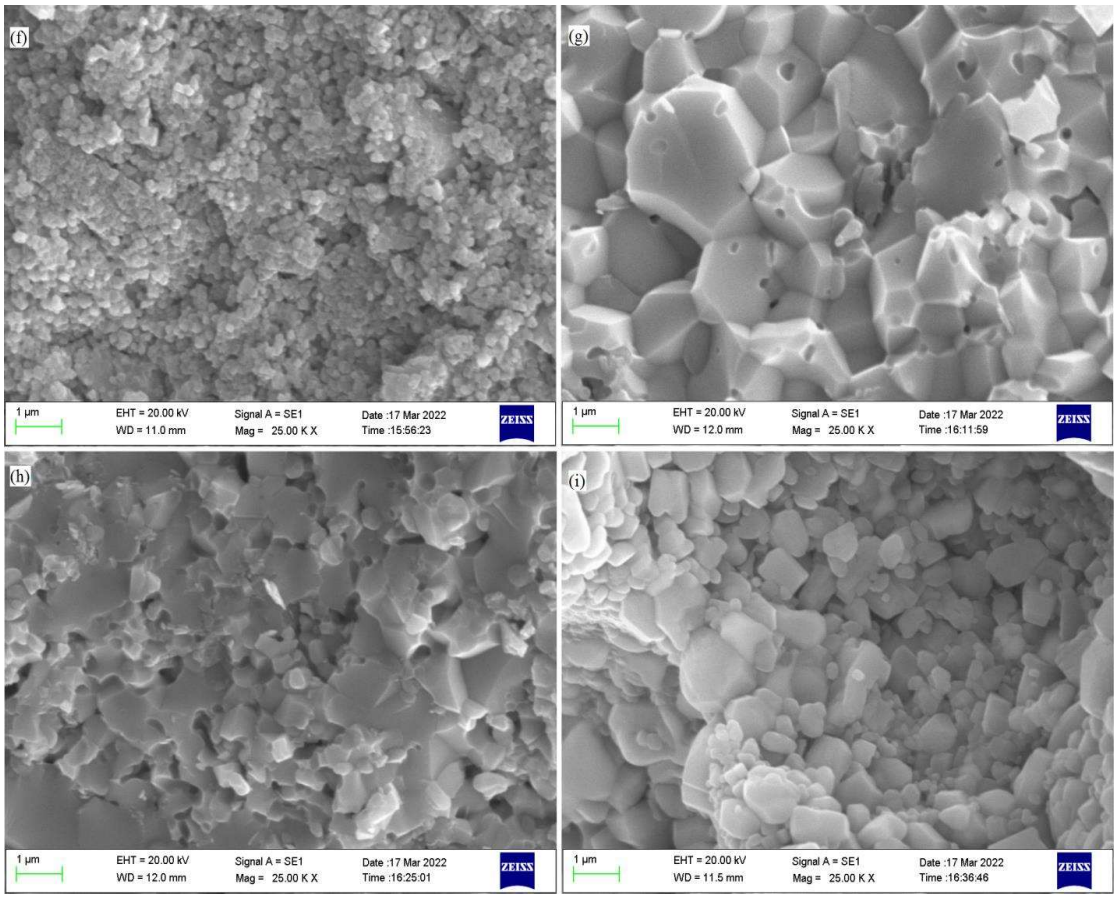


**Figure 4.2** SEM image of fractured surface of $BiY_{(1-x)}Mn_xO_3$ pellets sintered at 900°C for two hour (f) $x$ = 0.0 (g) $x$ = 0.10 and (h) $x$ = 0.25 (i) $x$ = 0.75.

All these micrographs clearly show the formation of well resolved grains and grain boundaries without any melted glassy region. The grain size for the fractured surface also follows the same trend as observed for the surface images of the pellets with changing composition. It should be noted that the composition with x=0.10 having larger grain size (1.07µm), exhibit transgranular fracture while the compositions with x=0, 0.25 and x=0.75 with smaller or bimodal grain size exhibit mostly intergranular fracture. The size of the larger grains is estimated to be 1.5 µm and smaller grains to be 0.5 µm for the compositions with x= 0.25, as determined from the SEM image of the fractured surface. Likewise the grains sizes are 0.9 µm and 0.6 µm for the compositions with x=0.75. Overall, increasing trend of grain size due to increased Mn concentration

is observed which supports lowering of the band gap, consistent with the previous reports in similar systems [188, 189].

### 4.3.3. XPS Analysis:

We have carried out a comprehensive x-ray photoelectron spectroscopy (XPS) analysis of $BiY_{(1-x)}Mn_xO_3$ samples to identify the elements, their oxidation states, ratio of oxidation states and concentration of oxygen vacancies in the sample. Figs. 4.3 (a, b, and d) show the narrow scan spectra of Bi-4f, Y-3d, Mn-2p and O-1s, respectively, for the composition with x=0.25 while Fig. 4.3(c) shows Mn-2p peak for the composition with x=0.50. The XPS survey of elements confirms the presence of Bi, Y, Mn and O in the chemical composition of the sample. Calibration of the narrow scan binding energy peaks were done by taking C1s peak (285.05 eV) as reference. Fig. 4.3(a) shows Bi4f doublet peaks for $Bi^{3+}f_{5/2}$ at 163.87 eV and $Bi^{3+}f_{7/2}$ at 158.57 eV corresponding to $Bi^{3+}$ state, confirming Bi to be present in only +3 oxidation state. Moreover, the spin orbit splitting energy of Bi4f can be estimated to be 5.3 eV from Fig. 4.3(a) which is similar to the previously reported values [190, 191]. The BE peak positions of Y3d are quite overlapping with the $Bi^{3+}f_{7/2}$ peak. As shown in Fig. 4.3(a), the deconvolution of the lower energy XPS peak around 158 eV, reveals the BE peak positions of Y3d at 159.16 eV and 157.71 eV belonging to the $Y^{3+}3d_{3/2}$ and $Y^{3+}3d_{5/2}$ respectively. Splitting energy of Y-3d is estimated to be around 1.5 eV confirming stable (+3) oxidation state of Yttrium ion also. As can be seen in Fig. 4.3(b), the intensity of the XPS spectra of Mn-2p is rather weak due to its lower concentration (x=0.25) in the sample. However, a clear asymmetric peak can be seen in the narrow scan of Mn-2p around 640 eV, which correspond to the Mn-$2p_{3/2}$, the high spin state of spin orbit coupling. Analysis of the XPS data for Mn-2p reveals that the two oxidation states of manganese, +3 and +2 are

present in the sample. The Mn-2p peak shown in Fig. 4.3(b) can be fitted by two peaks related to $Mn^{2+}$ $2p_{3/2}$ at 640.74 eV and $Mn^{3+}$ $2p_{3/2}$ at 642.28 eV. To further confirm the oxidation states of Mn, we show in Fig. 4.3(c) the BE doublet peaks of Mn-2p for the composition with x=0.50. The clearly resolved doublet peaks can be deconvoluted into four peaks corresponding to $Mn^{2+}$ $2p_{3/2}$ at 641.22 eV, $Mn^{3+}$ $2p_{3/2}$ at 644.24 eV, $Mn^{2+}$ $2p_{1/2}$ at 652.71 eV and $Mn^{3+}$ $2p_{1/2}$ at 654.13 eV. The splitting between the doublet peaks for $Mn^{2+}$(11.4 eV) and $Mn^{3+}$ (9.9 eV) are consistent to the splitting energy of the +2 oxidation states and +3 oxidation state of Mn reported earlier in similar systems [192]. A shift in the peak position of Mn-$2p_{3/2}$ with increase in Mn concentration can be seen which shows the successful incorporation of Mn in the solid solution [176, 191]. Analysis of the area under deconvoluted XPS peaks for both compositions (x=0.25 and x=0.50) reveal that $Mn^{3+}$ is the dominant oxidation state (~75-80%) while $Mn^{2+}$ is estimated to be ~ 20-25%. Hence XPS characterization of both compositions of $BiY_{(1-x)}Mn_xO_3$ with x=0.25 and x=0.5 reveals that Mn oxidizes in $Mn^{3+}$ and $Mn^{2+}$ states that have ionic radii of 0.645 Å and 0.96 Å, respectively whereas the ionic radii of $Bi^{3+}$ and $Y^{3+}$ are 1.17 Å and 1.019 Å respectively. For fluorite structure Bi/Y/Mn ions are expected to occupy same position constituting the cubic closed packed lattice and oxygen ions are expected to occupy tetrahedral sites. The significantly smaller size of the $Mn^{+3}$ in comparison to $Y^{+3}$ can increase the lattice distortion to make system less stable. To compensate for this, a sufficient fraction of $Mn^{3+}$ converts to $Mn^{2+}$ with bigger ionic size. The charge neutrality condition is expected to be met by the formation of the oxygen vacancies. Fig. 3(d) shows the Oxygen 1s BE energy peak, which can be deconvoluted to two peaks corresponding to the lattice oxygen ($O_I$) at 531.07 eV and oxygen vacancies ($O_{II}$) at 531.95 eV. Compositional ratio of lattice oxygen and Oxygen vacancies ($O_I$ : $O_{II}$ ) are estimated to be 63:37, showing 62% oxygen in lattice and

relatively large (37%) percentage of non-lattice oxygen [190]. Presence of such a large oxygen vacancy can be attributed to the relatively high concentration of $Mn^{2+}$ cation as discussed earlier, responsible for generating deficit of positive charge which is balanced by removal of anions.

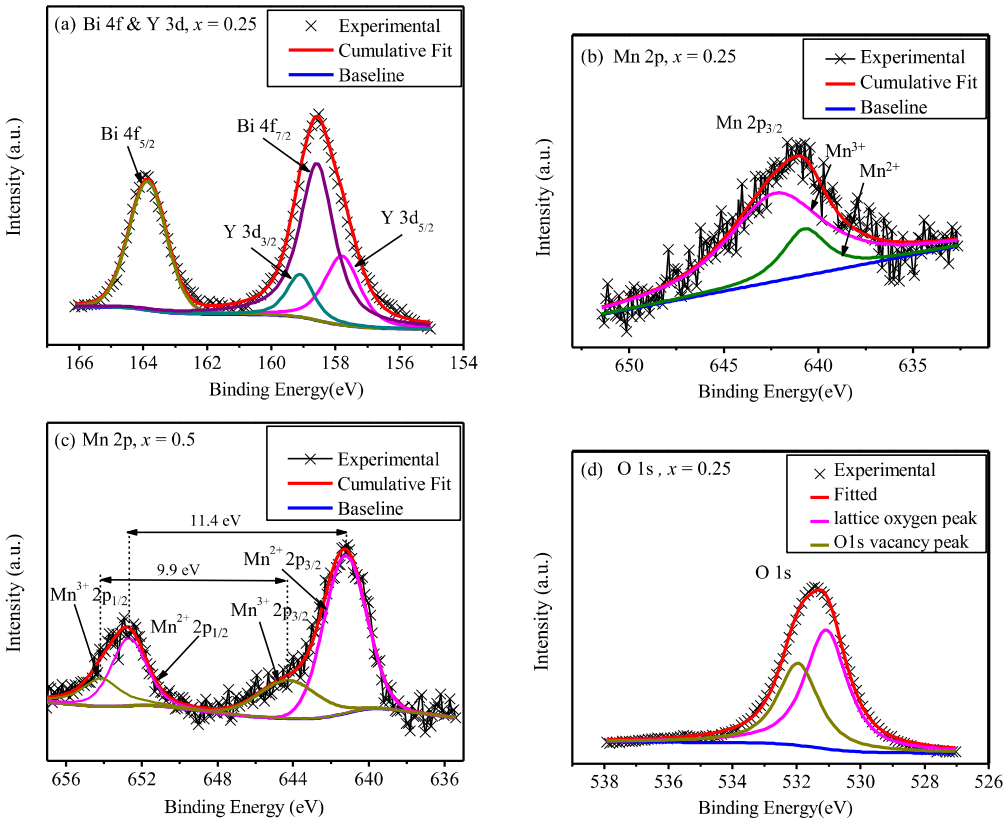


**Figure 4.3:** Fig. 4.3. XPS spectrum of (a) Bi-4f & Y-3d, (x = 0.25) (b) Mn-2p (x = 0.50) (c) Mn-2p (x = 0.25) and (d) O-1s (x = 0.25) for $BiY_{(1-x)}Mn_xO_3$ (x = 0.25) (Black cross: observed data; overlapping red line on data: cumulative fitted curve; solid blue line: background; magenta, violet, olive, and cyan lines: identification peaks).

### 4.3.4. Crystal Structure Analysis:

X-ray diffraction patterns of various $BiY_{(1-x)}Mn_xO_3$ samples calcined at 800°C for 4 hours are shown in Fig. 4.4(a) along with a zoomed portion of the diffraction pattern in Fig. 4.4(b). As can be seen in Fig. 4.4(a and b), the diffraction peaks shift on the lower two-theta side on increasing 'x' which indicates increased unit cell volume

with increasing Mn-concentration. The XRD patterns of the compositions with x=0, 0.10, 0.25 and 0.50 are similar in nature which suggests that the crystal structure is same for these compositions. The crystal structure of pure $BiYO_3$ is reported to be cubic (JCPDS card number 27-1047) in the *Fm*-3*m* space group [193]. Few very weak peaks labelled by asterisk (*) in Fig. 4.4(a) can be related to the peaks of a coexisting tetragonal phase which appears when calcination is not done at very high temperature, as reported earlier [194]. However, nearly pure cubic phase is obtained up to the composition with x=0.50. As shown in Fig. 4.4(b), increasing Mn concentration shifts the XRD peaks to the lower 2θ side which confirms the successful incorporation of 'Mn' at the 'Y' site along with the increased unit cell volume.

For the $BiY_{(1-x)}Mn_xO_3$ sample with x=0.75, large number of new XRD peaks appear in addition to the peaks corresponding to the cubic fluorite phase with space group *Fm*-3*m*. Analysis of the XRD pattern for this composition reveals that there are secondary phases along with the cubic fluorite phase. The perovskite tetragonal $BiMnO_3$ phase is reported by Brankovi´ et. al [31] in the samples prepared by mechanochemical synthesis method. These authors also obtained few secondary non-stoichiometric Bi–Mn–O phases e.g. $Bi_{12}Mn_4O_{10}$ (JCPDS-74-1096) and $Bi_{12}MnO_{20}$ (JCPDS-39-1105) with some traces of unreacted $Bi_2O_3$ along with the perovskite phase. Highly distorted perovskite monoclinic phase with *C*2 space group is reported in the samples prepared by high pressure synthesis method for $BiMnO_3$ [38]. However, none of the earlier reported structure or mixed phases for $BiMnO_3$ system, explains the XRD pattern of $BiY_{(1-x)}Mn_xO_3$ sample with x=0.75. More detailed investigations are required to characterize non-perovskite, unidentified secondary phases in the composition with x=0.75.

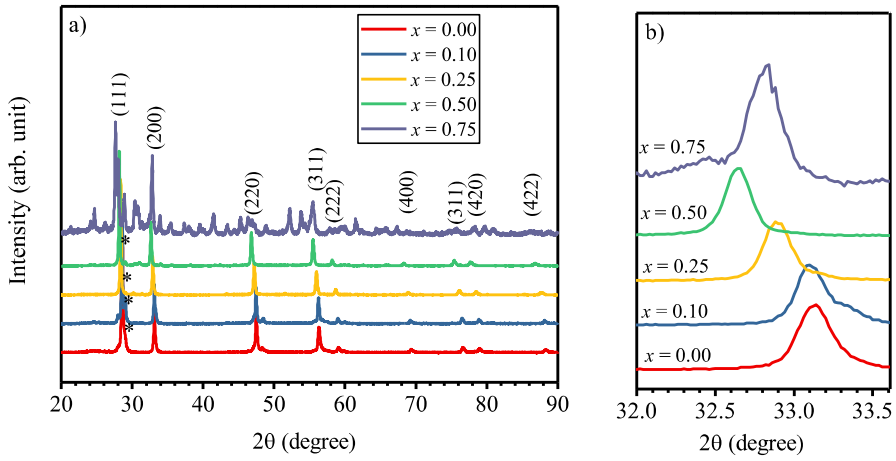


**Figure 4.4:** (a) X-ray diffraction pattern of $BiY_{(1-x)}Mn_xO_3$ ($x$ = 0.0, 0.10, 0.25, 0.50, 0.75 ) prepared by high energy ball milling method. Miller Indices are given for the cubic *Fm*-3*m* phase. (b) angular shift of the (200) peak with changing Mn concentration.

The cubic *Fm*-3*m* structure for the compositions with $x$ = 0.0, 0.10, 0.25 and 0.50 were further confirmed by Full pattern Le-Bail profile matching analysis. Very good fits for these four compositions are shown in the Figs. 4.5 (a-d) which confirm the cubic structure. The structure of composition with x=0.75 was difficult to refine due to presence of multiple phases with low symmetry. **Table 4.1** lists the lattice parameters, unite cell volume and $\chi^2$ factor. Lattice parameter shows an increasing trend in spite of substituting bigger $Y^{3+}$ (0.90Å) ion by relatively smaller cation $Mn^{2+}$ (0.83Å) /$Mn^{3+}$ (0.65Å), contrary to the Vegard's law which predicts decrease in the cell parameter for substitution by ion of smaller size. Here, instead of the ionic size, electron affinity and cell volume deformation play potential role in deciding unit cell volume [195]. Electron affinity of Mn (−0.50 eV) is much lower than Y (0.31 eV). When an element with relatively low electron affinity substitutes another element having higher electron affinity, it enhances the bond length and hence increases the lattice parameter, as reported earlier [41]. Such kind of unusual volume expansion is reported by Pengfei Jiang et. al., in solid solutions which have stereochemically active 6s lone pair electrons.

The possible explanation can be stated as 6s-6p orbitals of Bi may hybridize with the 3d orbital of Mn resulting in the release of strain associated with axial cell expansion [196].

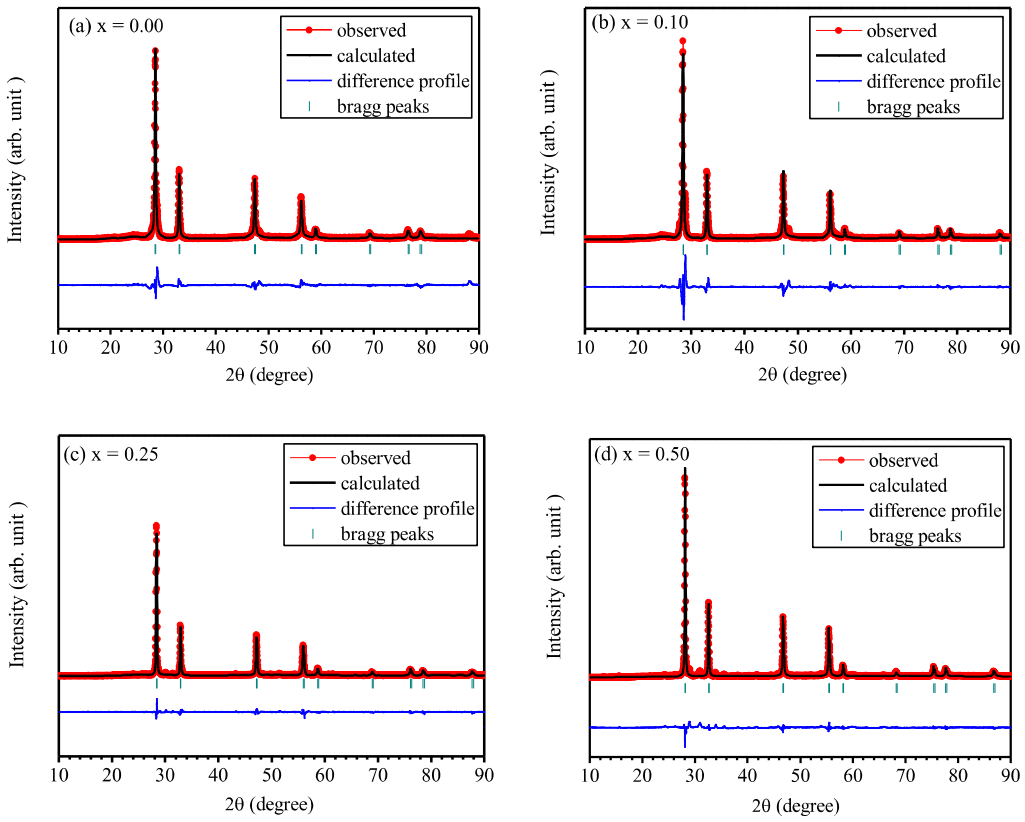


**Figure 4.5:** (a-d) Refinement fits for X-Ray diffraction pattern of $BiY_{(1-x)}Mn_xO_3$ ($x$ = 0.0, 0.10, 0.25, 0.50.

**Table 4.1:** Refined structural parameters for $BiY_{(1-x)}Mn_xO_3$ (x = 0.0, 0.10,0.25,0.50).

| **Composition $BiY_{(1-x)}Mn_xO_3$** | **a (Å)** | **Volume (Å$^3$)** | **$\chi$ 2** |
|---|---|---|---|
| x = 0.0 | 5.4233(5) | 159.51(3) | 4.57 |
| x = 0.10 | 5.4317(4) | 160.25(2) | 5.85 |
| x = 0.25 | 5.4460(5) | 161.52(6) | 2.65 |
| x = 0.50 | 5.4930(2) | 165.74(2) | 5.56 |

### 4.3.5. Dielectric Studies:

To analyse the dielectric behaviour of $BiY_{(1-x)}Mn_xO_3$, permittivity was characterized in the frequency range 100Hz-1kHz, from 40°C to 600°C temperature, through a programmable furnace with the measurement in the heating run at the rate of

2°C/min. Measurement of relative permittivity $\varepsilon_r$ (dielectric constant) was done by parallel plate capacitance method. Figs. 4.6(a, b, c, d and e) show the variation of real part of complex permittivity with increase in temperature. It is clear from the Figs. 4.6(a-d) that there is absence of any peak/anomaly in the temperature dependence of permittivity for the compositions x=0, 0.10, 0.25 and 0.50, showing absence of any phase transition. As discussed in previous section, XRD analysis reveals that up to the *x* = 0.50 Mn concentration, solid solution crystallizes in cubic structure, which is most symmetric phase and no further phase transition is expected with increasing temperature for these compositions. However, as shown in Fig. 4.6(e), for the compositions with x=0.75, temperature dependence of permitivity exhibits a weak peak around 375 °C, which can be attributed to the phase transition of monoclinic phase into another crystalline phase, as reported for $BiMnO_3$ [182, 183, 186]. Fig. 4.6(f) shows loss tangent at 1kHz for samples with x = 0.10, 0.25, 0.50 and 0.75 in the temperature range 40°C to 100°C. It is observed that loss tangent is below 1 at room temperature (~40°C) for all the Mn containing samples. Loss tangents have increasing trend with higher Mn concentration above 60°C. Below 60°C, the x=0.25 composition has higher loss tangent than x=0.50 which can also be observed in the slightly lossy shape of PE loops.

For all the prepared samples, value of dielectric constant is continuously increasing non linearly with temperature, starting from the room temperature value, it increases on average 10 to 20 times for every 100°C increment of temperature. For example, at 100°C temperature, order of dielectric constant was observed to be $10^1$-$10^3$ at 110Hz ($\varepsilon_r$ = 36, for x=0, $\varepsilon_r$ = 28 for x=0.10, $\varepsilon_r$ = 40 for x=0.25, $\varepsilon_r$ =290 for x=0.50 and $\varepsilon_r$ = 1200 for x=0.75) whereas at 600°C, it increased upto $10^6$ order (1.6 x $10^6$ for x=0.10, 2.2 x $10^6$ for x=0.25, 2.1 x $10^6$ for x=0.50, and 1.0 x $10^6$ for x=0.75).

Furthermore, rise in dielectric permitivity increases sharply after 400°C at all frequencies.

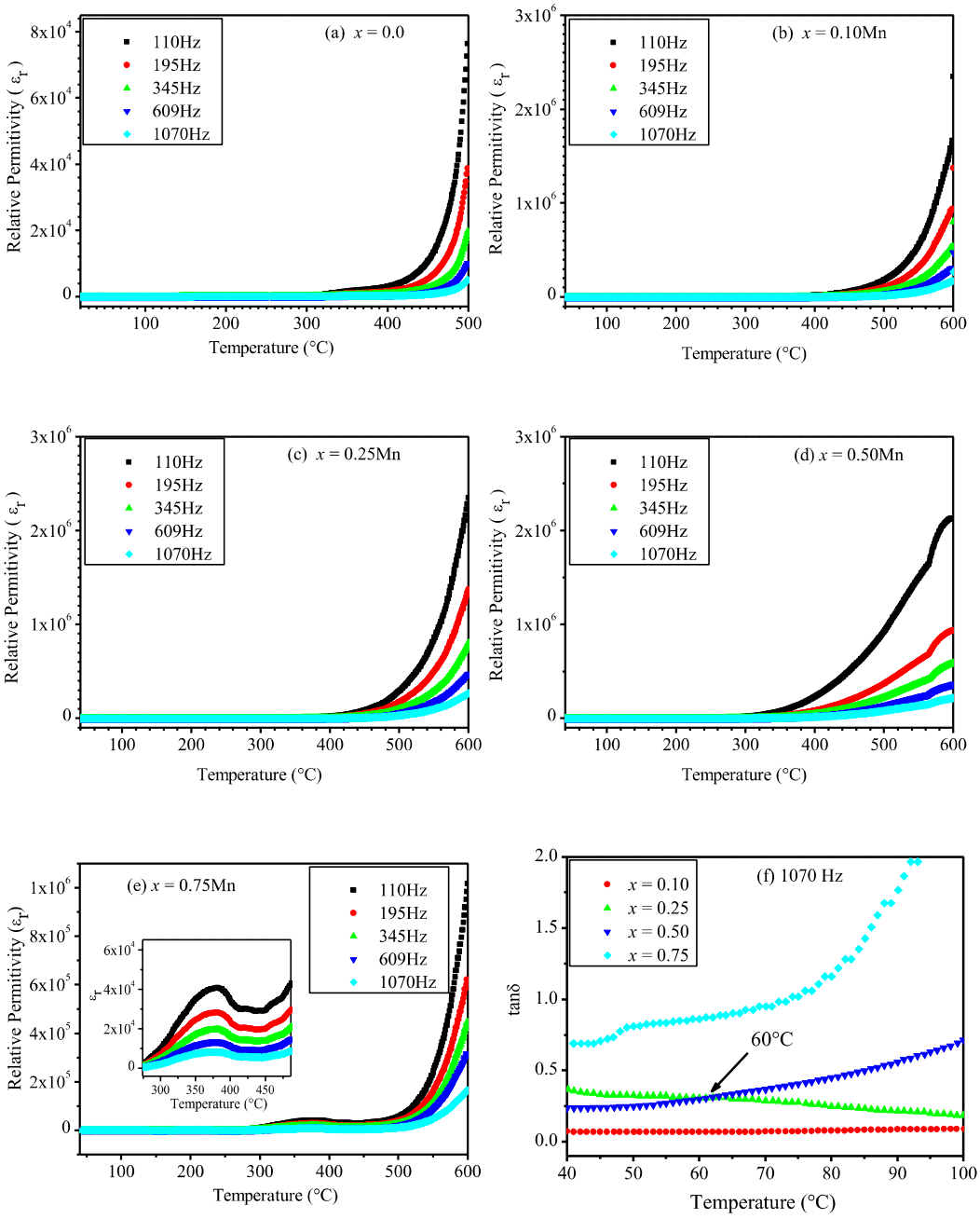


**Figure 4.6:** (a-e) Temperature-frequency dependence of relative permittivity for different compositions of $BiY_{(1-x)}Mn_xO_3$ ($x$ = 0.0, 0.10, 0.25, 0.50 and 0.75, respectively) (f) Loss tangent comparison of samples ($x$ = 0.10, 0.25, 0.50, 0.75) near room temperature.

The rate of increase in $\varepsilon_r$ is higher for lower frequencies due the phenomena of dipole relaxation, explained rigorously in several existing literature [148, 149]. Increase of dielectric constant with temperature is attributed to the increased conductivity as well as increased polarizability of ions, which results into increased permittivity at high temperatures. There are various other parameters affecting the dielectric properties such as oxygen vacancies, ratio of $Mn^{2+}$ to $Mn^{3+}$ ions, sintering temperature, grain size, grain boundaries and interfaces in the polycrystalline samples. Conclusively, it can be inferred that there is increasing trend in dielectric constant with increasing Mn- concentration in the solid solution, which suggests better polarization for these compositions.

**4.3.6. Complex Impedance Study**

Electrical transport properties of polycrystalline materials are amply determined by impedance spectroscopy. Impedance analysis of $BiY_{(1-x)}Mn_xO_3$ with $x$ = 0.0, 0.10, 0.25, 0.50 and 0.75 were done using impedance spectroscopy over the frequency range 20Hz to 1MHz, for temperature range 40°C to 300°C, in air atmosphere. Typically polycrystalline metal oxide samples are characterized by grains, separated by grain boundaries, which are relatively less conducting than grains [150, 151]. Contribution of the grains (bulk) and grain boundaries to the net impedance can be extrapolated by complex impedance plot between Z'' (reactive component of impedance) as Y-axis and Z' (resistive component of impedance) as X-axis, also known as Nyquist plot [151-153]. Figs. 4.7(a-e) show Nyquist plots at 200°C for $BiY_{(1-x)}Mn_xO_3$ with $x$ = 0.0, 0.10, 0.25, 0.50 and 0.75, respectively. All the plots show single semicircular arc with center lying below the real axis. Most of the arcs appear to pass through origin at higher frequencies and making positive intercepts at real axis in low frequency region for all the compositions. In the Nyquist plot for x = 0.75, the sum of grain and grain boundary resistance does not have very high value to dominate over the resistance due to contact.

Therefore, the points does not appear close to the origin. The sum of grain and grain boundary resistance (span of arc's real intercept) is of similar order as that of contact resistance (high frequency intercept). The equivalent circuit model for such behavior should be composed of at least a capacitor with loss (parallel RC circuit) corresponding to the semicircular curve. Single semicircular arc is obtained when total impedance is dominated by the impedance of any one of the three contributors (grain, grain boundary and electrode impedance). In present samples, electrode impedance is negligible and grain boundaries have very large resistance dominating over the grains resistance, resulting in a single semicircular curve [197, 198]. The intercept of semicircular arc at Z' axis, on the low frequency side, will determine the sum of the resistance of grains and grain boundaries. Compound resistance (Sum of grain and grain boundary resistances) and hence corresponding conductivity of the various compositions were estimated by Nyquist plot fitting using ZSIMP-WIN version-2 software and the obtained values are listed in **Table 4.2.** It is evident from **Table 4.2** that, conductivity of $BiYO_3$ is minimum and increases monotonically with Mn incorporation. DC conductivity ($\sigma$) of the polycrystalline bulk material can be estimated using formula $\sigma = \frac{L}{SR}$ ; where $S$ is the cross sectional area of the sample, $L$ represent the thickness and $R$ is the resistance of the grains respectively [156]. Applying the above formula, DC-conductivities of all the five samples were calculated and are listed in **Table 4.2**. It is evident that the arc radius of Mn-containing samples has become smaller with larger Mn concentration in $BiY_{(1-x)}Mn_xO_3$. It indicates that the resistance for the charge transport in $BiY_{(1-x)}Mn_xO_3$ is reduced with higher Mn concentration. The possible reasons for this reduction are the hopping phenomena of electrons at the $Mn^{2+}$, $Mn^{3+}$ sites, and increased oxygen vacancies. Moreover, increased oxygen vacancies shifts the conduction band towards the Fermi level and hence the carrier density in conduction band increases [199]. Thus,

incorporation of Mn promotes oxygen vacancies and also provides a path for charge transfer and hence greatly improves the conductivity of electrons and holes generated after photon absorption, consequently enhancing the separation efficiency of the photo current carriers.

Figs. 4.7(f) and 7(g) show the fitted Nyquist plots for $x$ = 0.10 and $x$ = 0.75, at different temperatures, 140°C, 160°C, 180°C and 200°C respectively. It is evident that radius of impedance plot semicircle decreases with increase in temperature, indicating decreased grain and grain boundary resistances at higher temperatures. This can be interpreted as presence of thermally activated conduction mechanism in the material. DC impedance and DC conductivity of $BiY_{(1-x)}Mn_xO_3$ for the compositions with x = 0.10 and x = 0.75, at different temperatures, 140°C, 160°C, 180°C and 200°C are listed in **Table 4.3.** Increased conductivity and lower DC impedance at higher temperatures is clear from the values given in this table. Such phenomenon is known as negative temperature coefficient behaviour (NTCR) revealing semiconducting nature of the material. Variation of dc-conductivity with the inverse of absolute temperature is shown in Fig. 4.7(h) following Arrhenius plot (i.e $\ln\sigma_{dc}$ versus 1000/T). Empirical formula $\sigma = \sigma_p e^{-E_a/kT}$ is used to explain the temperature dependence of conductivity, where $\sigma_p$ is the pre-exponential factor, $k$ Boltzmann constant and $E_a$ activation energy. The activation energy is calculated from the slope of the $\ln\sigma_{dc}$ versus 1000/T plot and the estimated values of activation energy for $BiY_{(1-x)}Mn_xO_3$ compositions with $x$ = 0.10, 0.50 and $x$ = 0.75 are 0.94 eV, 0.71 eV and 0.45 eV respectively. It can be seen that activation energy $E_a$ is decreasing with increasing Mn composition in $BiY_{(1-x)}Mn_xO_3$ solid solution. Activation energy $E_a$ lies in the range of 0.71-0.94 eV for $x$ = 0.10 to $x$ = 0.50 composition, whereas activation energy for composition with x = 0.75 (0.45 eV) is

significantly lower than other compositions. Hence the value of activation energy for all the compositions except x = 0.75 shows that electrical conduction is led by oxygen vacancy conduction mechanism whereas intermediate value of activation energy for x = 0.75 corresponds to the electron/hole-phonon interaction mechanism [200, 201].

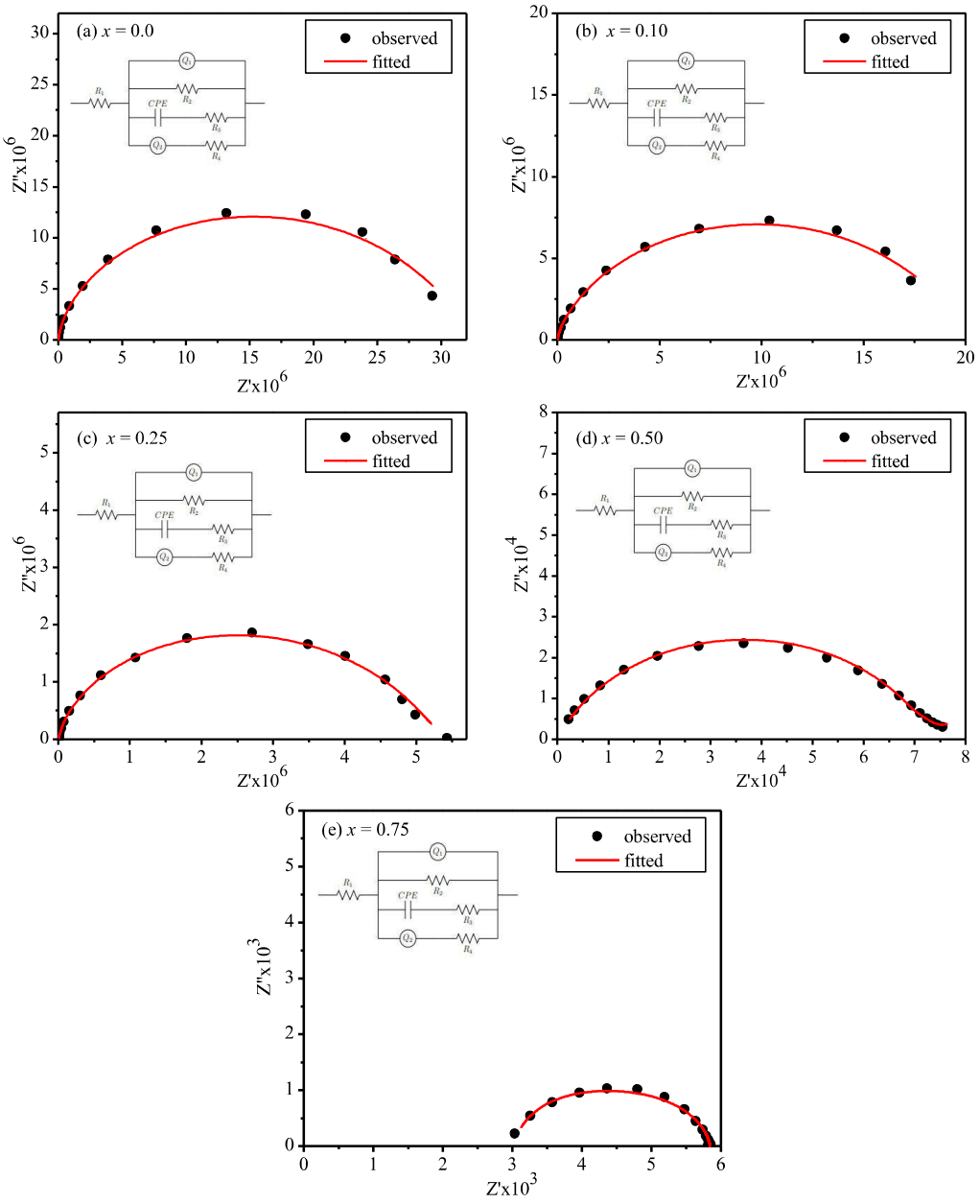


**Figure 4.7:** Fitted Nyquist plots between Z' and Z'' measured at 200°C for $BiY_{(1-x)}Mn_xO_3$ (a) $x = 0.0$ (b) $x = 0.10$ (c) $x = 0.25$ (d) $x = 0.50$ and (e) $x = 0.75$.

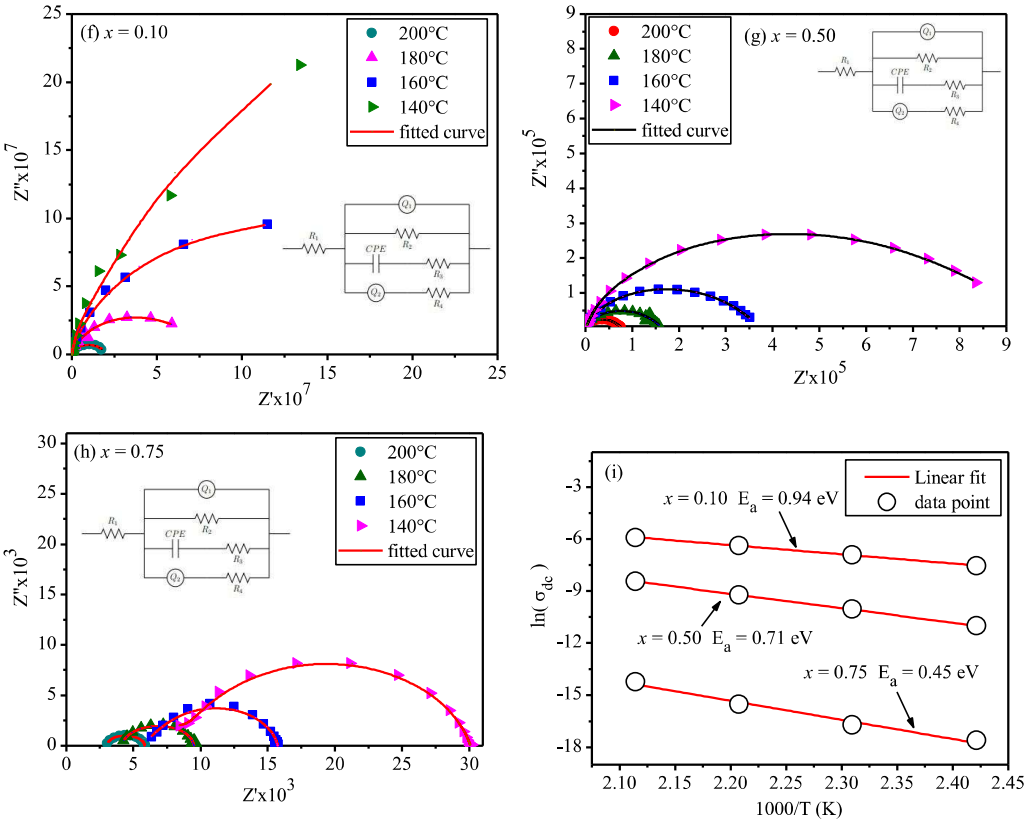


**Figure 4.7:** Nyquist plots at different temperatures for (f) $x = 0.10$, (g) $x = 0.50$ and (h) $x = 0.75$. (i) Arrhenius plot of dc conductivity for $x = 0.10$ , 0.50 and $x = 0.75$.

**Table 4.2:** DC impedance and DC conductivity of $BiY_{(1-x)}Mn_xO_3$ for different compositions.

| Composition | Compound Resistance $R_g + R_{gb}$ ( Ω ) | DC Conductivity $\sigma$ (S/m) |
|---|---|---|
| $x = 0.0$ | 3.3 x $10^7$ | 4.3 x $10^{-7}$ |
| $x = 0.10$ | 2.1 x $10^7$ | 6.7 x $10^{-7}$ |
| $x = 0.25$ | 5.4 x $10^6$ | 2.5 x $10^{-6}$ |
| $x = 0.50$ | 7.5 x $10^4$ | 2.1 x $10^{-4}$ |
| $x = 0.75$ | 5.8 x $10^3$ | 2.7 x $10^{-3}$ |

**Table 4.3.** DC impedance and DC conductivity of $BiY_{(1-x)}Mn_xO_3$ ($x$ = 0.10, $x$ = 0.75) at various temperatures.

| Composition | Temperature (°C) | Compound Resistance $R_g + R_{gb}$ ( Ω ) | DC Conductivity $\sigma$ (S/m) |
|---|---|---|---|
| $x$ = 0.10 | 200 | 2.1 x $10^7$ | 6.7 x 10-7 |
| | 180 | 7.8 x $10^7$ | 1.8 x 10-7 |
| | 160 | 25.4 x $10^7$ | 5.5 x 10-8 |
| | 140 | 61.6 x $10^7$ | 2.3 x 10-8 |
| $x$ = 0.50 | 200 | 7.5 x $10^4$ | 2.1 x 10-4 |
| | 180 | 1.6 x $10^5$ | 1.0 x 10-4 |
| | 160 | 3. x $10^5$ | 4.3 x 10-5 |
| | 140 | 9.7 x $10^5$ | 1.7 x 10-5 |
| $x$ = 0.75 | 200 | 5.8 x $10^3$ | 2.7 x 10-3 |
| | 180 | 9.5 x $10^3$ | 1.7 x 10-3 |
| | 160 | 15.7 x $10^3$ | 1.0 x 10-3 |
| | 140 | 30.1 x $10^3$ | 5.3 x 10-5 |

### 4.3.7. Ferroelectric Characterization:

Figs. 4.8 (a-e) show the polarization ($P$) versus applied electric field ($E$) hysteresis plots (P-E loop) measured at room temperature and 200Hz frequency, for $BiY_{(1-x)}Mn_xO_3$ with $x$ = 0.0, 0.10, 0.25, 0.50 and 0.75, respectively. In Figure 4.8(f), hysteresis loops of different compositions are plotted together for better comparison. The thickness of samples for P-E loop measurements was taken to be about ~1mm and the maximum field applied was 40 kV/cm at constant frequency of 200 Hz. It can be noted that polarization does not saturate with increasing applied electric field and curve of the P-E loops is gradually rounded at high field region due to slightly lossy nature. At high temperature (above 300K) it was difficult to measure good quality P-E loops due to the high leakage current. Breakdown was observed when applied field goes beyond 45 kV/cm field. From Figs. 4.8(a-d), it can be clearly observed that maximum polarization increases with increasing electric field for each composition. However, a lossy, and square shaped P-E loop is observed for x=0.75 composition which has significant Mn-concentration and consequently large leakage current due to electrons hopping conduction at the $Mn^{2+}$, $Mn^{3+}$ sites.

Fig. 4.8(a) shows the ferroelectric behavior of $BiYO_3$. It illustrates that remanent polarization ($P_r$) and coercive field ($E_c$) both are increasing with increasing applied field (E) but saturation is not observed up to 40 kV. For increment of 5 kV/cm field, remanent polarization, on an average, increases by 0.016 μC/cm$^2$ and coercive field by ~2.9 kV/cm. Similar increasing pattern of $P_r$ and $E_c$ were observed with increase in applied electric field for x=0.10, 0.25 and 0.50 samples shown in Figs. 4.8(b, c, d). For these samples, average increase in $P_r$ per 5 kV/cm increment in electric field are 0.015 μC/cm$^2$, 0.035 μC/cm$^2$ and 0.039 μC/cm$^2$ with increasing field while average increase in $E_c$ is almost same about ~2.8 kV/cm. Fig. 4.8(f) demonstrates the visual comparison of P-E loops of various compositions. It can be seen that that P-E loops are tending towards rounded shape at higher concentration of Mn (x value) and higher $P_r$ value is observed with increasing concentration of Mn ($x$ value) for compositions with x=0.10, 15 and 0.20. However, exceptionally high apparent remanent polarization and coercive field, even higher than composition x=0.50, is observed in x=0.25 due to relatively high leakage current as inferred by the lossy shape of the PE loop. If the leakage effect is excluded, remanent polarization value $P_r$ (0.23 μC/cm$^2$) for composition with x=0.50 will be highest in all the four compositions. This composition also shows highest value of polarization (0.48 μC/cm$^2$) at 40 kV/cm field. These values of polarizations are better than the previously reported polarizations for polycrystalline (i) pure $BiMnO_3$ at room temperature $P_r$ = 0.06 μC/cm$^2$ [202] and $P_r$ = 0.043 μC/cm$^2$ at 200 K [172] (ii) pure $BiFeO_3$ $P_r$ = 0.06 μC/cm$^2$ at room temperature [203]. Increased Mn concentration in $BiY_{(1-x)}Mn_xO_3$ will enhance Jahn-Teller distortion promoting tilting of the rigid $Y/MnO_6$ block unit which will favour the enhancement of polarization [57, 204]. Conclusively, incorporation of Mn will enhance the polarization in modified system. Moreover

presence of yttrium is reported to reduce the volatilization of Bi-oxide which also leads to improved ferroelectricity [205].

The crystal structure analysis of the investigated samples ($x$ = 0.0, 0.10, 0.25, 0.50 except $x$ = 0.75) reveals that major phase as cubic, while P-E loop measurements reveal ferroelectric nature. This indicates an improper ferroelectric behaviour of these samples. Various models are given to understand the phenomena of improper ferroelectricity but a clear and detailed explanation is still awaited. Ku Xe et. Al. reported trilinear coupling mechanism to understand and design the improper ferroelectrics in perovskite and non-perovskite structures. They suggested that substitution of suitable cation/anion can break the local inversion symmetry of a centrosymmetric structure (e.g. cubic) creating possibility of ferroelectric behavior [206]. Many compositions of (1-x)$BiFeO_3$-x$BaTiO_3$ (0.3 < x < 0.4) [207], (0.94−x)$Bi_{0.5}Na_{0.5}TiO_3$–0.06$BaTiO_{3-x}K_{0.5}Na_{0.5}NbO_3$ (0 < x < 0.11) [208], 0.6$BaTiO_3$-0.4$BiScO_3$ [209] and $BaTiO_3$-$Bi(Mg_{1/2}Ti_{1/2})O_3$-$BiFeO_3$ [210] are the series of the materials that crystalize in average cubic structure but show weak ferroelectric behaviour due the local deviation from the cubic symmetry. In present case, a cubic fluorite structure with non-similar three elements, lone pair of Bi at A-site, partial local ordering of off-centered Bi-ions, change in local atomic structure under electric field and small tilting of the rigid Y/$MnO_6$ block units may be the possible cause for appearance of ferroelectricity [57, 207, 208, 211, 212]. Thus following these reports, it can be concluded from Fig. 4.8 that all the samples exhibit ferroelectric behavior and optimal incorporation of Mn improves ferroelectricity.

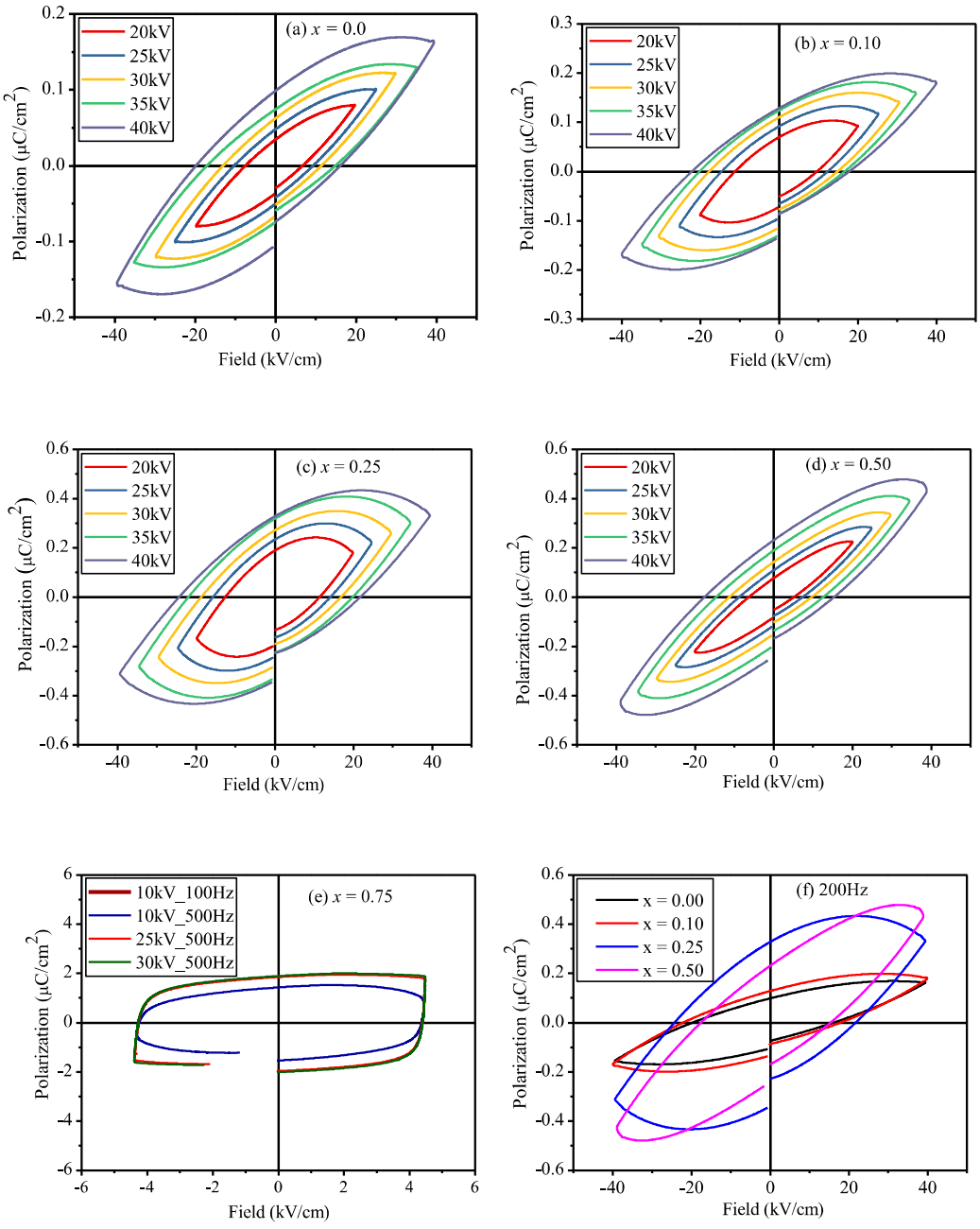


**Figure 4.8:** Room temperature P-E loops measured at different field strength at 200Hz for $BiY_{(1-x)}Mn_xO_3$ (a) $x$ = 0.0 (b) $x$ = 0.10 (c) $x$ = 0.25 (d) $x$ = 0.50 (e) $x$ = 0.75 and (f) combined P-E loops of $BiY_{(1-x)}Mn_xO_3$ ($x$ = 0.0, 0.10, 0.25, 0.50) compositions measured at 200Hz and 40 kV/cm.

### 4.3.8. Band Gap Analysis:

Fig. 4.9(a) shows the optical absorption curves for $BiY_{(1-x)}Mn_xO_3$ with $x$ = 0.0, 0.10, 0.25, 0.50 and 0.75, evaluated from the Kubelka-Munk equation of the UV-Vis diffuse reflectance spectra. Fig. 4.9(b), shows Tauc Plot for various compositions along with estimated band gaps. In Tauc Plot, $(\alpha h\nu)^n$ is plotted against photon energy ($h\nu$) where n is the constant associated with the type of electronic transition, n = 2 for direct band gap while n = ½ for indirect band gap semiconductor [127]. The Mathematical expression for relationship of absorption coefficient $\alpha$ and direct band gap $E_g$ can be given by $(\alpha h\nu)^2 = A(h\nu - E_g)$ ; where A is band tailoring constant and $h\nu$ is photon energy. As shown in Fig. 4.9(b), the linear part of the absorption curve is extrapolated up to the x-axis and the point of intersection determines the bandgap. It is evident from Fig. 4.9(b), that the Tauc plot of two compositions x=0.0 and 0.10 exhibit single absorption edge and only one linear region while the other three compositions $x$ = 0.25, $x$ = 0.50 and $x$ = 0.75 have two linear absorption regions inferring two absorption edges and band gaps. Similar double absorption edge resulting in huge change in optical structure were reported recently in $BaTiO_3$-$_xBaCo_{0.5}Nb_{0.5}O_{3-\delta}$ [166]. Main absorption edge or band gap energy of $x$ = 0.0, 0.10, 0.25, 0.50 and 0.75, were estimated to be 3.05 eV, 2.71 eV, 2.67 eV, 1.76 eV and 2.0 eV respectively. Variation of band gap and lower absorption edge with Mn- concentration ($x$) for $BiY_{(1-x)}Mn_xO_3$ is shown in Fig. 4.9(c). It is observed that band gap curve has a minimum at (x=0.50) while the second absorption edge starts at x=0.25 and decreases monotonically. The band gap is observed to be successively decreasing from 3.05 eV ($x$ = 0.0) to 1.76 eV ($x$ = 0.50) with increasing Mn concentration except for the composition with x=0.75 (2.0 eV), where main absorption edge is increased to higher energy than main absorption edge of 0.50. However, the lower absorption edge of x=0.75 is observed to be 1.33 eV which is the

lowest absorption edge amongst all the samples. Due to the second absorption edge, compositions x=0.25, 0.50, and 0.75 have broader absorption range that penetrates to far IR region with absorption edges at 1.48 eV, 1.46 eV and 1.33 eV respectively. Conclusively, increasing Mn substitution in $BiY_{(1-x)}Mn_xO_3$ solid solution, not only reduces the band gap remarkably from 3.05 eV ( $x$ = 0.0 ) to 1.76 eV ( $x$ = 0.50 ) but it also enhanced the absorbance range of radiation.

There are various mechanisms explaining such kind of reduction in band gap. It can be predicted on the basis of previous studies that in $BiYMnO_3$, Y-4d orbitals form the conduction band (CB), whereas, valence band (VB) can be formed by either of Bi-2s, O-2p, Mn-3d orbitals or all these orbitals hybridized together [199]. Presence of small fraction of $Mn^{2+}$ ions promote formation of oxygen vacancies and conduction band is reported to shift with creation of oxygen vacancies that is consistent with the XPS and UV analysis [199]. Increasing the Mn-concentration may result in formation of more defects that promote extended tailing in the absorption curve, hence, reduction in the band gap. Dopant incorporation to oxide crystals leads to generation of several meta stable states [213, 214]. Existence of these metastable states allows intermediate transitions attributing to the wavelength absorption in wider range [215]. Zu-Zeng et. al. have reported that the area under the absorption curve of the $BiYO_3$ is relatively more than the other Bi containing perovskites without Yttrium. Thus, presence of Y-element in $BiY_{(1-x)}Mn_xO_3$ also contributes to the increased absorptivity in wider wavelength range [179].

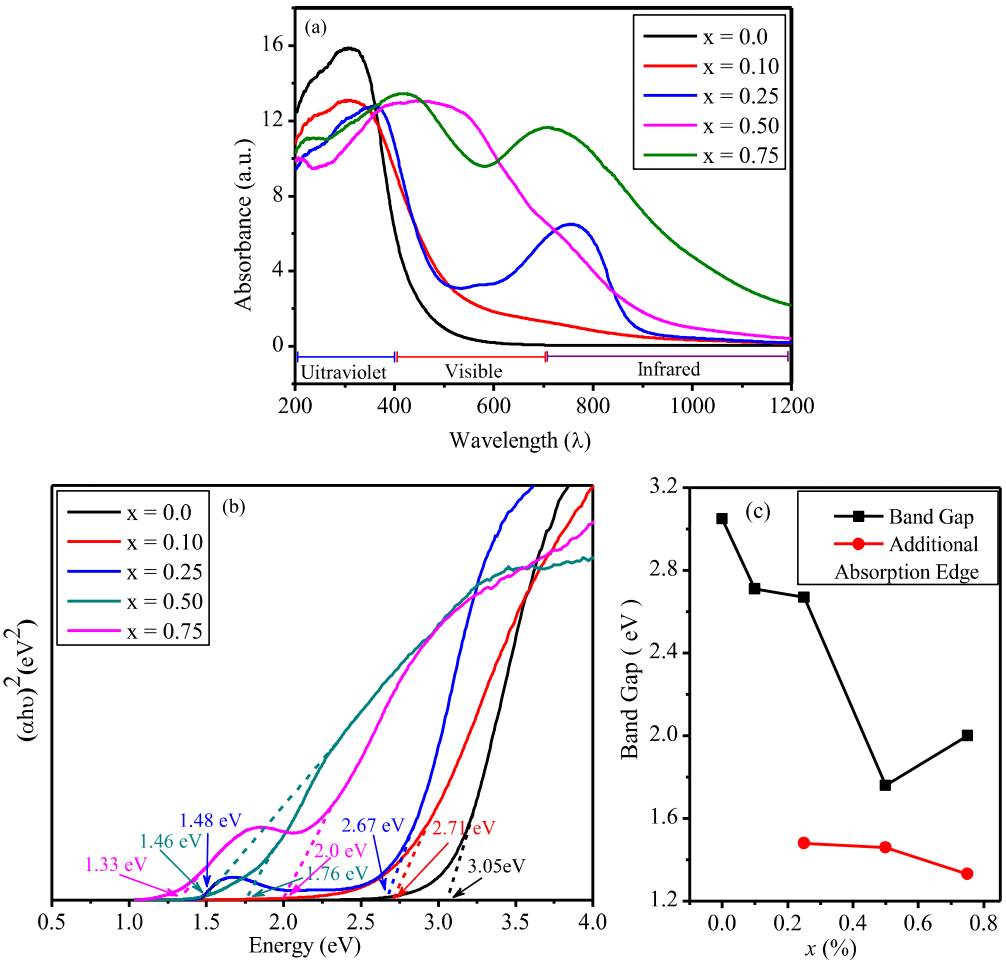


**Figure 4.9:** Fig. 4.9. (a) Optical absorption curves, (b) Tauc plots with extrapolated band gap and (c) Composition dependence of band gap, for $BiY_{(1-x)}Mn_xO_3$ ceramics

## 4. 4 Conclusions

Structural, morphological, dielectric, optical, electrical and ferroelectric properties of $BiY_{(1-x)}Mn_xO_3$ ($x$ = 0.0, 0.10, 0.25, 0.50 and 0.75) solid solution have been studied in detail on samples prepared by high energy ball milling method. X-ray analysis reveals that all the samples except $x$ = 0.75, crystallize into cubic fluorite structure and lattice parameter increases with increase in Mn concentration. Incorporation of Mn also enhances the dielectric constant leading to better polarizability

of the material. Both the grains and grain boundary resistances reduce significantly with increase in Mn concentration as well as with rise in temperature showing an enhanced conductivity of charge carriers. Band gap is successfully achieved to lower value (lowest 1.76 eV for $x$ = 0.50) along with a minor additional absorption edge at 1.33 eV ( $x$ = 0.75 ). The lowest band gap (1.76 eV) achieved in Mn substituted $BiYO_3$, is better than Mn doped $BiFeO_3$ (1.92 eV). P-E hysteresis loops confirm the ferroelectric behavior for all the samples and enhancement in polarization is observed for solid solution with higher Mn concentration. Conclusively, we have developed novel oxide material $BiY_{(1-x)}Mn_xO_3$ compositions which are ferroelectric, and have adequately low band gap, suitable to utilize wider wavelength range of the solar spectrum. It can be a promising material for solar cell and thermoelectric applications.